Novel Multiferroic-Like Nanocomposite with High Pressure-Modulated Magnetic and Electric Properties

Chunrui Song, Wei Xu, Nikita Liedienov,* Igor Fesych, Roman Kulagin, Yan Beygelzimer, Xin Zhang, Yonghao Han,* Quanjun Li, Bingbing Liu, Aleksey Pashchenko,* and Georgiy Levchenko*

In this work, a novel multiferroic-like nanocomposite is designed and obtained using the high-pressure torsion (HPT) method. The crystal structure, phase composition, morphology, ferromagnetic (FM), and ferroelectric (FE) properties of the initial powders and ferroelectric/ferromagnetic nanocomposites are studied comprehensively. The initial powders and their composite show the perovskite and spinel crystalline phases for the FE and FM fractions, respectively. After HPT, the particle sizes of the initial powders are decreased significantly. It is shown that the novel nanocomposite consists of exchange-interacting FE and FM phases and demonstrates improved magnetic and electrical properties in low fields at room temperature. A giant increase in residual polarization with an increase in external high-pressure is found in new composite. The obtained results make it possible to consider the novel nanocomposite as a new functional material for its use both in electronic devices for monitoring ultra-high-pressure and in integrated circuits of high-speed computing nanosystems with low switching energy. The HPT method is a promising method for obtaining new heterophase nanosystems.

1. Introduction

Multiferroics are a new class of multifunctional materials where magnetic, electric, and elastic orderings coexist.[1] The coexistence of magnetostrictive and piezoelectric properties is the reason for the appearance of the magnetoelectric (ME) effect.[2] The increased interest in the designing and research of such new materials is due to their multifunctionality and practical application.[3] Based on the ME effect, supersensitive sensors of alternating and constant magnetic fields operate with more million times higher sensitivity than the Hall sensors.[4] The preservation of magnetostrictive properties in the microwave range is the basis for the creation of the latest technology for wireless energy transfer to miniature electronic devices.[5] Multilayer film heterostructures based on multiferroics have a high potential for use in high-speed storage devices with low energy consumption and high memory density.[6] Layered composite materials that suppress pyroelectric noise without averaging the useful signal are employed in the development of the latest high-sensitivity $\approx 10^{-12}$ T and low-frequency $\approx 10^{-2}$–10^3 Hz sensor technologies for non-invasive neurological interfaces in medicine.[7]

Currently, the rapid development of modern technologies requires more and more new multiferroic materials including composites with improved characteristics and unique manufacturing methods. The idea of creating a new composite is to find the phase and chemical composition of the heterophase system, which will respond to the improved functional properties for its practical application. It is advisable to consider the phase composition of the "ferroelectric–ferromagnetic," where the ferroelectric (FE) is La-modified $Bi_{0.9}La_{0.1}FeO_3$ (BLFO) multiferroic bismuth ferrite, and the ferromagnet (FM) is $Mn_{0.6}Zn_{0.3}Fe_{2.1}O_4$ (MZFO) manganese–zinc ferrospinel. Multiferroic BLFO has

C. Song, N. Liedienov, X. Zhang, Y. Han, Q. Li, B. Liu, A. Pashchenko, G. Levchenko
State Key Laboratory of Superhard Materials
International Center of Future Science
Jilin University
Changchun 130012, P. R. China
E-mail: nikita.ledenev.ssp@gmail.com; hanyh@jlu.edu.cn; alpash@ukr.net; g-levch@ukr.net
W. Xu
State Key Laboratory of Inorganic Synthesis and Preparative Chemistry
College of Chemistry
Jilin University
Changchun 130012, P. R. China

N. Liedienov, Y. Beygelzimer, A. Pashchenko, G. Levchenko
Donetsk Institute for Physics and Engineering named after O.O. Galkin
NAS of Ukraine
Kyiv 03028, Ukraine
I. Fesych
Taras Shevchenko National University of Kyiv
Kyiv 01030, Ukraine
R. Kulagin
Institute of Nanotechnology
Karlsruhe Institute of Technology
76021 Karlsruhe, Germany
A. Pashchenko
Institute of Magnetism
NAS of Ukraine and MES of Ukraine
Kyiv 03142, Ukraine

a high temperature of FE and FM orderings, as well as large electrical polarization values. The MZFO ferrospinel is a high-permeable magnetic ferrimagnet with a large initial magnetic permeability $\mu = 3000$, a high Curie temperature $T_C = 501$ K, a small coercivity $H_C = 0.25$ Oe, and the large saturation magnetization $M_S = 88$ emu g^{-1}.[8] It means that in small magnetic fields $H \approx 1$–100 Oe ($H > H_C$) a t r oom t emperature, t he m agnetic induction $B = \mu H$ may reach large values on the MZFO FM interface if MZFO particles are in a single-domain state. The critical size of the single-domain state D_0 for Mn–Zn ferrospinel is in the range $D_0 = 20$–30 nm.[9] For soft magnetized MnFe$_2$O$_4$ ferrospinel with close magnetic characteristics, the exchange length is $l_{ex} \approx 2$ nm.[10] If the BLFO–MZFO nanocomposite consisting of close-packed ultrafine particles with a size of $d < 20$ nm and with a width of interfacial boundaries less $l_{ex} \approx 2$ nm can be synthesized, a new material will be obtained with a high probability of linear ME effect in the range of weak fields. In the new heterophase system, the FM phase of the single-domain MZFO regions located at a distance smaller than the FM exchange length will affect r egions o f t he B LFO F E p hase w ith a s ize of a smaller than a period of spin cycloid by an external magnetic induction increased in $\mu = 3000$ times. Owing to the influence of a strong FM phase, we will have a large resulting magnetic moment, which can be easily controlled by ME coupling.

Creating new FE materials based on nanocomposites is the most promising method for obtaining new multiferroics with a large value of ME coupling.[2,11] Nowadays, most of the metal-oxide ceramic composites are obtained by mechanical mixing of powders with their sintering at the final stage.[12] However, this method is not suitable for our purpose, since the achievement of full consolidation at high sintering temperatures leads to a significant increase in grain size.[13] With the growth of grain, it may occur both the appearance of spin cycloids in the bismuth ferrite and a multi-domain state in the ferrospinel. In addition, at high sintering temperatures as a result of thermal dissociation, irreversible changes in the valence and spin state of manganese and iron are started with the degradation of the magnetic properties.[14] Therefore, the high-pressure torsion (HPT) method[15] for obtaining nanocomposite has been chosen, where full compaction of the heterophase system is accompanied by a statistically uniform distribution of phases in a bulk sample without changing the valence and spin state of magnetic ions.[16] The promising influence o f the various ceramics processed by HPT is presented in works.[17]

The optimal relationship between the amount of FE and magnetic phases is necessary to find during designing a nd synthesizing a new composite in addition to the determination of the chemical and phase composition. Since the key phase is the FE phase, the number of BLFO particles should exceed the amount of MZFO particles. The quantitative composition of the BLFO–MZFO nanocomposite consisting of 80 wt.% BLFO and 20 wt.% MZFO corresponds to the model for the binary system,[18] where the free space between the close-packed large BLFO particles of the multiferroic is filled with smaller MZFO particles of the ferromagnet. Necessary conditions for the implementation of such a model are the bigger size of the BLFO particles at least three times than the MZFO particles.

The purpose of this work is to create and study a new composite nanomaterial with improved magnetic and electric properties, which simultaneously will have a great value of electric polarization, and a large magnetic moment, as well as an appearance of FE and FM orderings above room temperature. The possibility of easy control of magnetic and electric properties in the range of weak magnetic fields will allow us to obtain new functional material for its wide application in many scientific, technical, and medical applications.

2. Results and Discussion

2.1. Morphology and Structural Properties

According to the X-ray diffraction (XRD) data (**Figure 1**), the initial BLFO and MZFO powders are fully single-phase. The XRD data indicate already a complete crystallization in the MZFO powder at 200 °C without additional annealing. The broadening of the diffraction maxima for the MZFO is due to the ultra-dispersity of the powder (Figure 1b).

The crystal structure of the BLFO powder has a rhombohedral $R3c$ distortion of perovskite structure (JCPDS No. 01-086-1519) with the $a = 5.57321$ Å and $c = 13.78585$ Å (Supporting Information S1) parameters of the unit cell. The
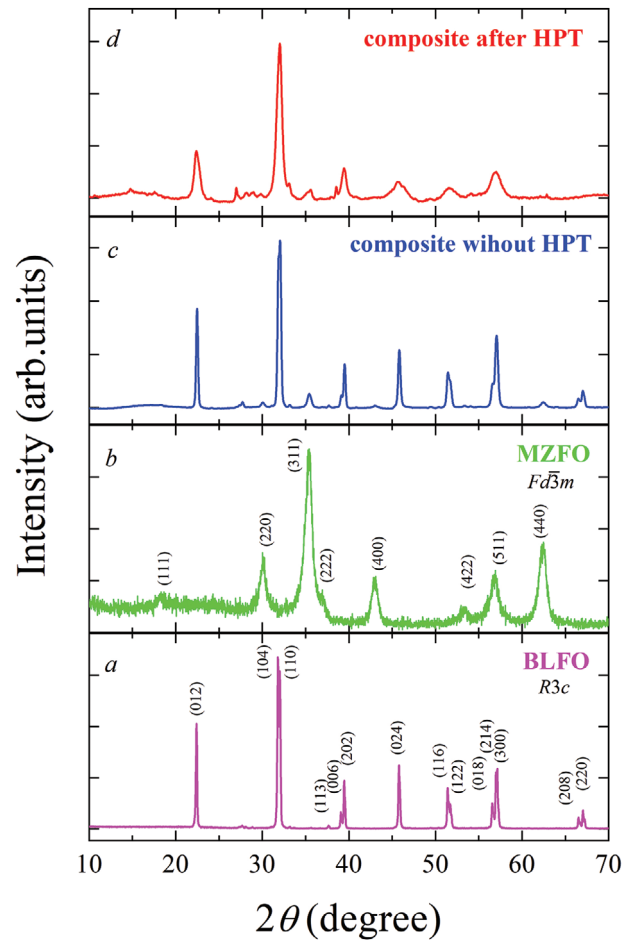
Figure 1. XRD patterns of the a) BLFO and b) MZFO initial powders, as well as the BLFO–MZFO composite processed by c) compression and d) HPT.

Table 1. Comparative analysis of XRD, transmission electron microscopy (TEM), and scanning electron microscopy (SEM) data for the structural parameters of the initial BLFO and MZFO powders, as well as BLFO–MZFO composite processed by compression and HPT.

Sample		D_{XRD} [nm]		D_{TEM} [nm]	D_{SEM} [nm]	$\varepsilon \cdot 10^4$
		Scherrer	Williamson–Hall			
BLFO powder		131	104	158	370	6.6
MZFO powder		15	13	15	–	1.5
BLFO–MZFO composite	BLFO fraction	103	97	75 (70%) and 143 (9%)	–	5.4
	MZFO fraction	15	14	15 (21%)	–	2.7
BLFO–MZFO composite HPT	BLFO fraction	14	15	13	–	39
	MZFO fraction	12	15	12	–	19.6

MZFO powder has a cubic $Fd\overline{3}m$ spinel structure (JCPDS No. 96-230-0585) with the unit cell parameter of $a = 8.40195$ Å. The X-ray density determined from the XRD data is 8.217 and 5.238 g cm^{-3} for the BLFO and MZFO powders, respectively. The main crystallographic parameters of the initial BLFO and MZFO powders refined by the Rietveld method are shown in Table S1.1 (Supporting Information).

The XRD pattern of the BLFO-MZFO composite HPT (Figure 1c) corresponds to a combination of the XRD patterns from the initial BLFO and MZFO powders (Figure 1a,b). A distinctive feature of the XRD pattern for the BLFO–MZFO composite HPT (Figure 1d) is the X-ray line broadening due to a decrease in the crystallite size. An average crystallite size D_{XRD} in powders and composites was calculated by the X-ray line broadening method using both Scherrer[19] and Williamson–Hall approaches in Supporting Information S2. Both methods give comparable D_{XRD} values to each other (see **Table 1**). In the initial powders, the D_{XRD} is 104–131 nm for the BLFO powder and 13–15 nm for the MZFO powder. In a two-phase BLFO–MZFO composite, the size of the BLFO fraction decreased to 97–103 nm, while the size of the MZFO fraction was almost the same. In the BLFO–MZFO composite HPT, there was a severe decrease in the size of the multiferroic BLFO fraction to 14–15 nm and a slight reduction in the size of the FM MZFO fraction to 12–15 nm. Such a decrease in the size of BLFO and MZFO fractions is the result of fragmentation of the large BLFO particles with a hardness of ≈2.5 GPa[20] by the small MZFO particles with a higher hardness of ≈5.5 GPa[21] during plastic deformation of the HPT. Additionally, the microstrains ε were also estimated (see Supporting Information S2). As turned out, the microstrains ε of crystal structure for the composite after the HPT increases significantly compared to the initial powders and composite processed by compression because of the action of tensile forces. Moreover, the discrepancy among the lattice plane distances of the studied samples obtained during comparison of the high-resolution TEM (HRTEM) data (see below) and JCPDS PDF 2 cards (database) is reduced and achieves the minimum for the composite HPT. It additionally confirms the increase in the stress strains caused by the tensile forces.

According to TEM data (**Figure 2** and Supporting Information S3), the initial BLFO and MZFO powders consist of spherical-like particles with a size of $D_{TEM} = 158$ and 15 nm, respectively, which are consistent with the D_{XRD} values (see Table 1). Moreover, the BLFO and MZFO samples demonstrate well crystalline structure according to the selected area electron diffraction (SAED) pattern (see upper inserts of Figure 2) with an interplane distance of 0.382 nm (012) for the perovskite phase and 0.483 nm (111) for the spinel phase (see bottom inserts of Figure 2). Obtained data confirm the beginning of the spinel structure crystallization at low temperatures of ≈200 °C. Additional synthesis at higher temperatures leads to growing the particles and increasing their crystallinity (see Supporting Information S1). This is the important result for nanotechnology and nanomagnetism since additional annealing at higher temperatures can lead both to significant grain growth with standing beyond the nanoscale phenomena,[22] and a change in the ion valence states with declining the functional properties of the magnetic materials.[23]

Using TEM data (**Figure 3**, top), it can be seen that the BLFO–MZFO composite corresponds to a mixture of BLFO and MZFO powders, where the size of the MZFO particles maintains, and the size of the BLFO particles decreased by half after compression. The percentage of particles with $D_{BLFO} = 75$ nm (89%) and 143 nm (11%) have been determined by approximating the $n(D)$ dispersion by the Gaussian function, considering the normalization condition of $\int_{0}^{+\infty} n(D)dD = 1$ (Figure S3, Supporting Information).

However, significant changes in the BLFO-MZFO composite HPT (Figure 3, bottom) have occurred. First, the HRTEM images show a more than ten times decrease in the size of the BLFO fraction from $D_{TEM} = 158$ to 13 nm, which is in good agreement with XRD data (see Table 1). Second, the BLFO and MZFO fractions were compacted very tightly that led to weakly distinguishable shades in TEM images for the multiferroic and FM phases. For the accurate determination of the size of the BLFO and MZFO fractions, the differences in the values of interplanar distance according to the HRTEM images were used. Analysis of HRTEM images made it possible to estimate the width of the interphase boundaries of ≈1 nm. In the next section, a comparison of the width of the interphase boundaries with the FM exchange length l_{ex} will play important role in improving the magnetic and electric properties for a composite of close-packed multiferroic and FM fractions as a result of induced ferromagnetism into FE region from the FM region.

According to the scanning electron microscopy (SEM) data (**Figure 4** and Supporting Information S3), the BLFO–MZFO composite (Figure 4e) is a combination of the large BLFO with $D_{SEM} = 370$ nm (Figure 4a) and small MZFO (Figure 4c) particles. The large size of D_{SEM} compared to D_{XRD} and D_{TEM} is due to the adhesion.[24] At the same time, the BLFO–MZFO composite
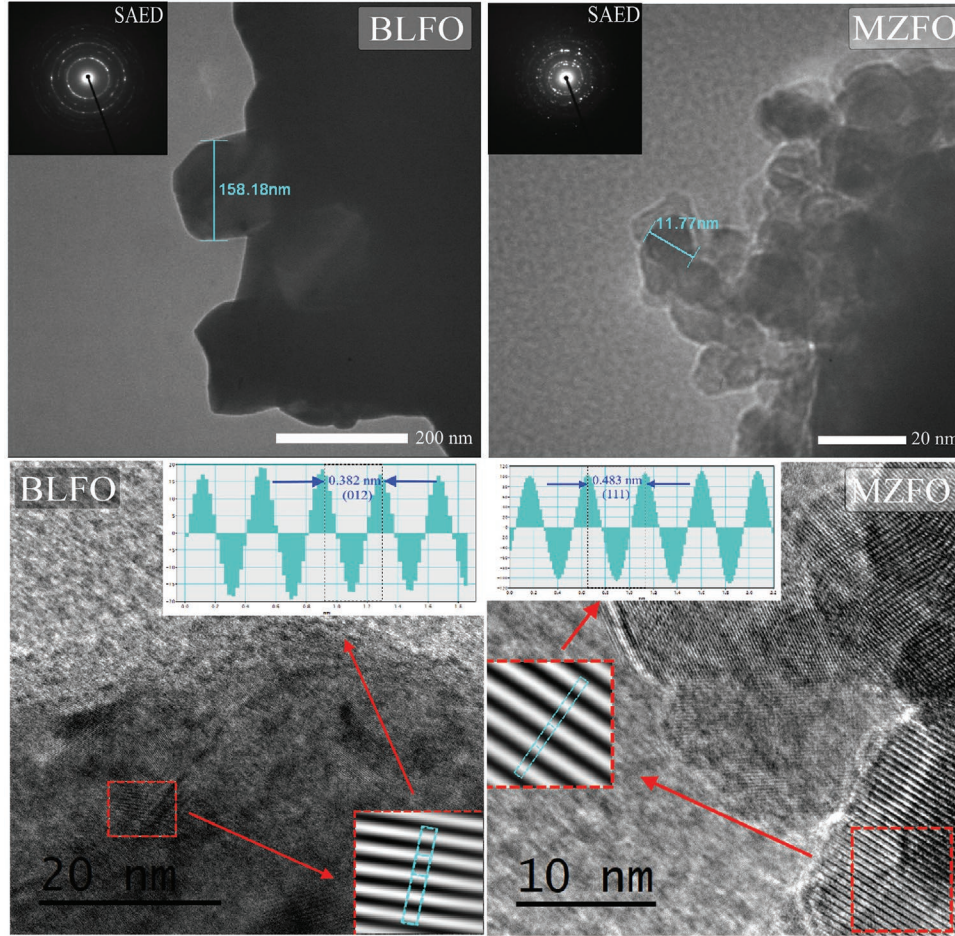
Figure 2. The TEM and HRTEM images for the initial BLFO and MZFO powders. The inserts show SAED and the fast Fourier transformation (FFT) of the HRTEM images with the lattice plane intensity profile.

HPT is well compacted and has a homogeneous microstructure without clear boundaries (Figure 4g).

According to the energy-dispersive X-ray spectroscopy (EDS) data, the chemical composition of the BLFO and MZFO powders, as well as both BLFO–MZFO composites, is confirmed, which corresponds approximately to the stoichiometric composition of $Bi_{0.9}La_{0.1}FeO_3$ and $Mn_{0.6}Zn_{0.3}Fe_{2.1}O_4$ and their combinations (Figure 4 and Supporting Information S4).

Thus, using HPT is an effective and promising method for obtaining heterophase nanostructures consisting of close-packed, ultra-dispersed, and uniformly distributed multiferroic and FM phases. HPT results in i) a statistical uniform distribution of fractions in the sample; ii) reducing the size of phases due to the fragmentation of the particles by others with a higher microhardness that can be controlled by the number of revolutions; iii) decreasing the width of the interphase boundaries until to several unit cell periods at the close-packed phases.

2.2. Magnetic Properties

The temperature dependences of the magnetization $M_{ZFC}(T)$ and $M_{FC}(T)$ for the initial BLFO powder indicate the antiferromagnetic (AFM) nature of the interactions (Figure S5.1, Supporting Information).[7a] High values of coercivity $H_C \approx$ 2.2–2.4 kOe and remanent magnetization $M_r \approx$ 0.035 emu g^{-1} in the range of room temperatures (see **Table 2**) compared to $H_C \approx$ 0.003 kOe and $M_r \approx$ 0.0005 emu g^{-1} for the model multiferroic $BiFeO_3$ with cycloidal AFM[25] mean the destruction of the spin cycloid in the AFM iron sublattice by lanthanum ions. The appearance of hysteresis in the field dependences of $M(H)$ (see Figure S5.2, Supporting Information) is associated with the presence of weak FM in the BLFO powder.[26]

The temperature and field dependences of the $M_{ZFC}(T)$, $M_{FC}(T)$, and $M(H)$ for the initial MZFO powder (see Supporting Information S5) show its highly permeable soft FM nature (Table 2). The Curie temperature $T_C =$ 518 K (see the inset of Figure S5.1, Supporting Information) is above the room temperature and coincides with T_C for Mn-Zn ferrospinels of industrial grades 3000HMC (USSR), 3C91 (Germany), ML27D (Japan), which have the same stoichiometric composition and a large initial magnetic permeability $\mu =$ 3000.[8,23,27] As the temperature increases, the magnetic parameters decrease from $H_C =$ 365 Oe, $M_S =$ 88 emu g^{-1}, and $M_r =$ 26 emu g^{-1} at $T =$ 2 K to $H_C \approx$ 50–80 Oe, $M_S \approx$ 50 emu g^{-1}, and $M_r =$ 2–3 emu g^{-1} for the entire range of room temperatures from 300 to 400 K. Such
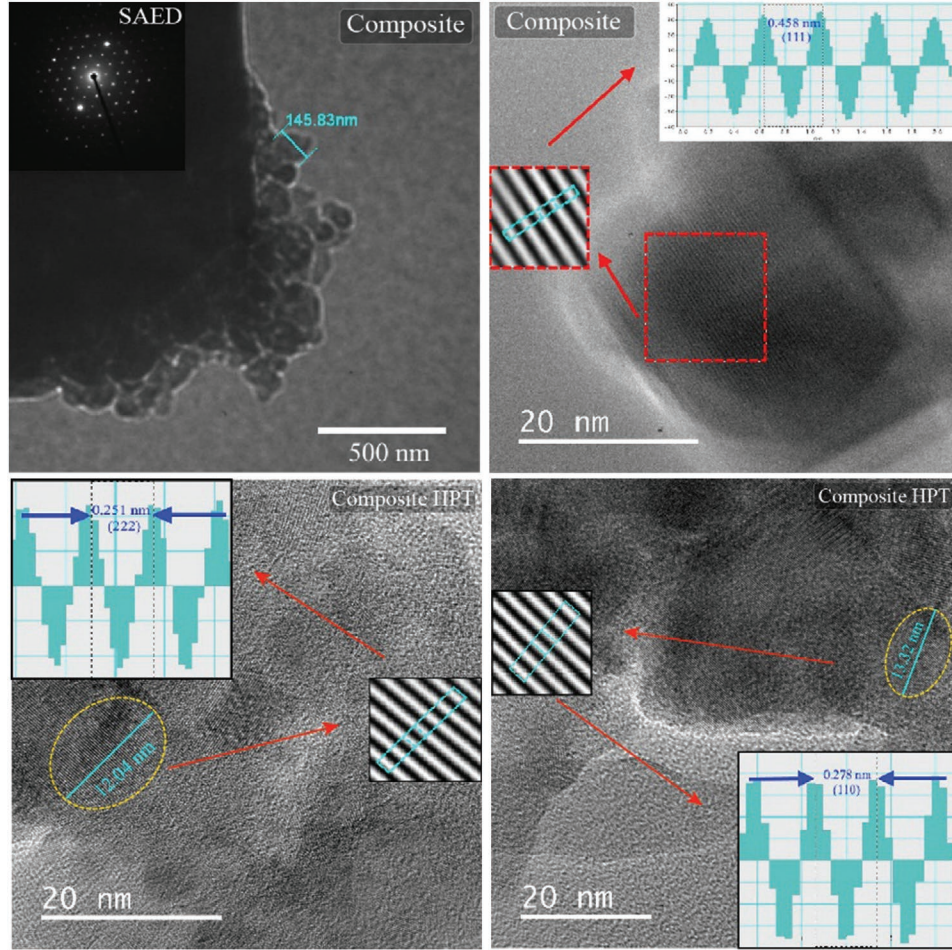
Figure 3. The TEM and HRTEM images for the BLFO–MZFO composite (top) and BLFO–MZFO composite HPT (bottom). The inserts show SAED, and the FFT of the HRTEM images with the lattice plane intensity profile.

magnetic characteristics make it possible to easily control the magnetic properties of FM high-permeability MZFO powder with $\mu = 3000$ by relatively small magnetic fields $H \approx 50–100$ Oe.

Figure 5 shows the $M_{ZFC}(T)$, $M_{FC}(T)$, and $M(H)$ dependences for both BLFO–MZFO composites processed by compression and HPT under external pressures of $p = 0$ and 1 GPa. First, we consider the magnetic properties of the composites under ambient pressure. For the BLFO–MZFO composite, with the increase in the temperature, the coercivity and magnetization decrease (see Table 2). The $T_C = 518$ K has not changed. The non-monotonic behavior of the $H_C(T)$ at room temperature is due to the presence of two uncompensated AFM sublattices in the ferrospinel with different temperature dependences of magnetization.[28] Analyzing the magnetic properties, it was found that the BLFO–MZFO composite did not exhibit individual features and its magnetic characteristics correspond to the additive contribution of magnetic properties from 80 wt.% BLFO and 20 wt.% MZFO.

Compared to the composite, the BLFO–MZFO composite HPT showed the properties of new material (Figure 5 and Table 2): i) the T_C has significantly decreased from 518 to 367 K that is additionally confirmed by the Arrott plots with a complex magnetic behavior of a second-order phase transition

(see Supporting Information S5); ii) the behavior of the $H_C(T)$ became monotonic for the entire room temperature range with a stabilized valued of $H_C \approx 35$ Oe; iii) a new FM order appeared at $T_C^* = 778$ K; iv) an anomalous hysteresis appeared between the $M_{ZFC}(T)$ and $M_{FC}(T)$ dependences, where the zero-field cooling (ZFC) curve is above the field cooling (FC) curve in the temperature range from 671 to 795 K; v) in the $M_{FC}(T)$ in contrast to the $M_{ZFC}(T)$ dependence, there are no signs of FM ordering at T_C^*; the residual magnetization reduces to $M_r \approx 0.04–0.4$ emu g^{-1} without a significant reduction in the $M_S \approx 3$ emu g^{-1} at the room temperature. It is necessary to note that the residual magnetization M_r is increased 12.5 times from $M = 0.032$ to 0.4 emu g^{-1} and the coercivity is decreased 65 times from $H_C = 2275$ to 35 Oe upon $H = 30$ kOe in the BLFO–MZFO composite HPT compared with the BLFO at $T = 300$ K. Moreover, the calculated value of the induction of the magnetic field $B = \mu H$ can take large values of ≈ 15 T on the border of the MZFO fraction with $\mu = 3000$ and $H = 50$ Oe in the new composite. However, the B cannot exceed the saturation induction B_S when all magnetic moments of iron are aligned along with the H. For the MZFO powder with the $M_S = 88$ emu g^{-1} and a density of 5.238 g cm^{-3} (see Table 1 and Table 2), the $B_S = 4\pi \times 10^{-4} M_S$ (emu cm^{-3})[29] equals
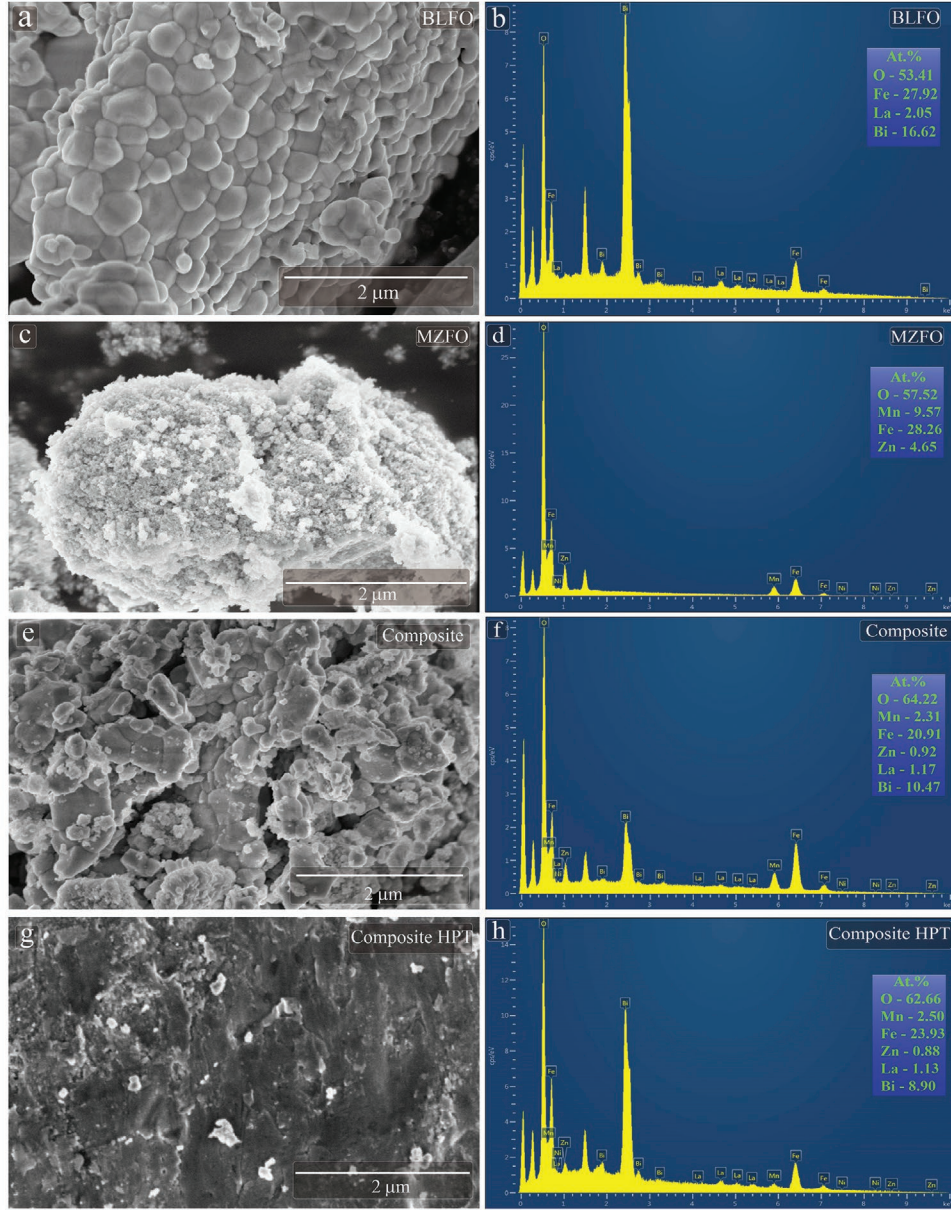
Figure 4. The SEM and EDS data for the initial BLFO and MZFO powders, as well as the BLFO–MZFO composite processed by compression and HPT.

0.58 T. Such B_S value is well consistent with the experimental value of $B_S = 0.525$ T for the manganese ferrospinel, which has an uncompensated total magnetic moment 4.2 μ_B in the ferrimagnetic iron sublattice.[30] The appearance of the $B = 0.58$ T in the composite means that the FM MZFO fractions with $\mu = 3000$ even in a small $H \approx 50$ Oe will induce a large inner $H_{int} \approx 5800$ Oe acting on the FE BLFO fraction.

Additionally, we studied the influence of high hydrostatic pressure of $p = 1$ GPa on the magnetic properties of both composites (see Figure 5c,d). As turned out, the pressure p trends to reduce the magnetic H_C, M_S, and M_r parameters of the composites at different temperatures (see Table 2) modifying bond angles Fe–O–Fe and bond distances Fe–Fe, and, consequently, the strength of AFM–FM exchange interactions.[31]

The results obtained at room temperature are of particular interest. Both the composites under $p = 1$ GPa demonstrate totally opposite behavior compared with the samples under ambient pressure. For the BLFO–MZFO composite, the pressure p increases the H_C by 42%, reduces the M_S by 23% and remains the M_r whereas for the BLFO–MZFO composite HPT the H_C and M_r are decreased by 23% and 50%, respectively, and the M_S is increased by 7%. It should be noted that such changes in magnetic properties of both composites will be correlated with the change in their polarization properties at room temperature (see "2.3. P-E properties" below). As it was shown for the ferrospinel Fe_3O_4,[32] the lower charge carrier density, the higher resistivity and lower saturation magnetization.

Table 2. The coercivity H_C, saturation magnetization M_S, and remanent magnetization M_r for the initial BLFO and MZFO powders, as well as BLFO–MZFO composite and composite HPT depending on the external pressure p.

| Sample		BLFO			MZFO			Composite				Composite HPT			
T [K]		2	300	400	2	300	400	2	77	300	400	2	77	300	400
H_C [Oe]	0	1150	2275	2425	365	55	82	352	135	7	23	337	127	35	34
	1 GPa	–	–	–	–	–	–	428	93	12	–	278	135	27	–
M_S [emu g^{-1}]	0	–	–	–	88	59	47	16	15	11	8	9	8	3	0.4
	1 GPa	–	–	–	–	–	–	13.3	13	8.5	–	7.4	7.1	3.2	–
M_r [emu g^{-1}]	0	0.02	0.03	0.04	26	2	3	5	2	0.2	0.4	3	2	0.4	0.04
	1 GPa	–	–	–	–	–	–	2.9	1.5	0.2	–	1.2	0.7	0.2	–

The existence of interactions between FM MZFO and FE BLFO fractions in the BLFO–MZFO composite HPT indicates anomalous temperature hysteresis on the $M_{ZFC}(T)$ and $M_{FC}(T)$ dependencies within the 671–795 K (Figure 5). Anomalous behavior of the ZFC curve above the FC curve is due to an additional FM contribution to magnetization when the composite is heated from the low-temperature FM region and the absence of this contribution when it is cooling from its high-temperature paramagnetic (PM) region. The MZFO fraction is the FM below $T_C = 367$ K. The BLFO fraction is the AFM below $T_N = 660$ K, FE below the temperature $T_C = 950$ K, and paraelectric (PE) above this temperature.[33] The phase state of the BLFO–MZFO composite HPT can be represented as: FM/(AFM+FE) $\leftarrow$ $(T_C = 367\,\text{K}) \rightarrow$ PM/(AFM+FE) $\leftarrow$ $(T_N = 660\,\text{K}) \rightarrow$ PM/(PM+FE) $\leftarrow$ $(T_C = 950\,\text{K}) \rightarrow$ PM/(PM+PE).

The anomalous appearance of the FM contribution in the PM/(PM+FE) phase (see the inset in Figure 5) is a consequence of a metamagnetic phase transition[7a,34] in the FM/(AFM+FE)
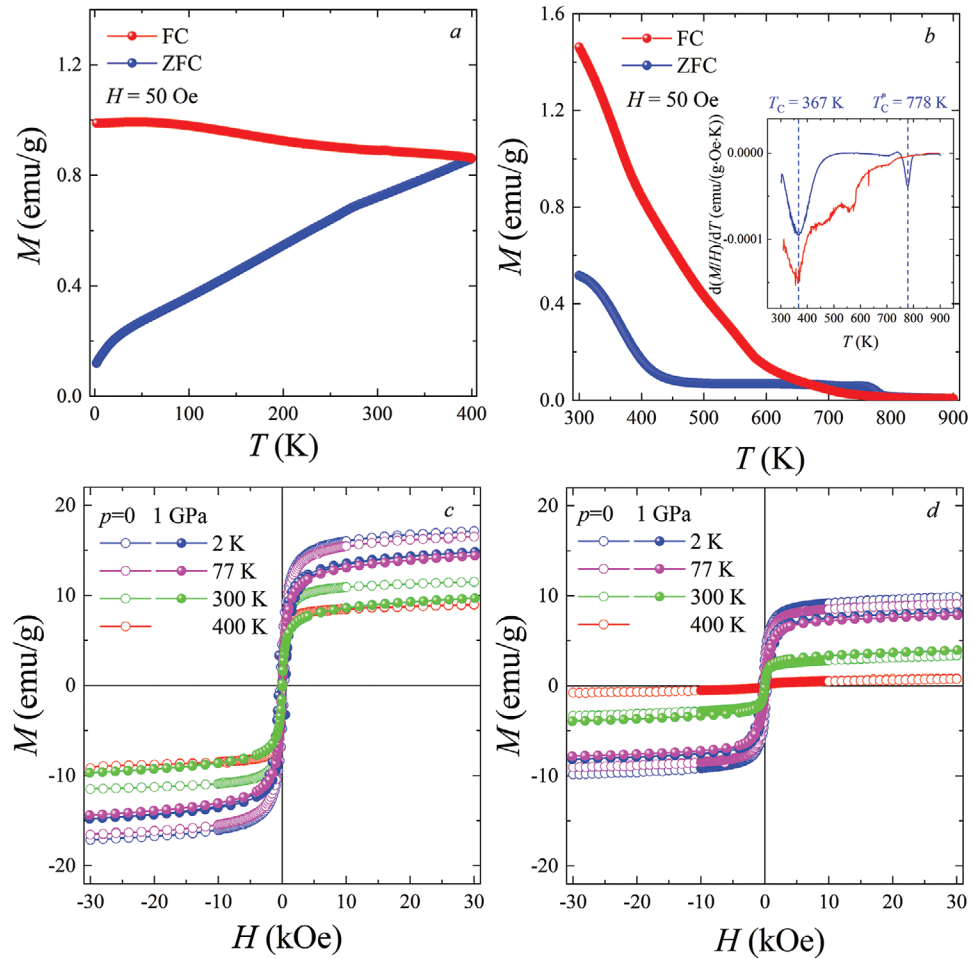
Figure 5. a,b) The $M_{ZFC}(T)$ and $M_{FC}(T)$ temperature dependencies and c,d) $M(H)$ field dependencies of the magnetization under different pressures $p = 0$ and 1 GPa for the composite (a and c) and composite HPT (b and d). The inset shows the Curie temperature T_C.
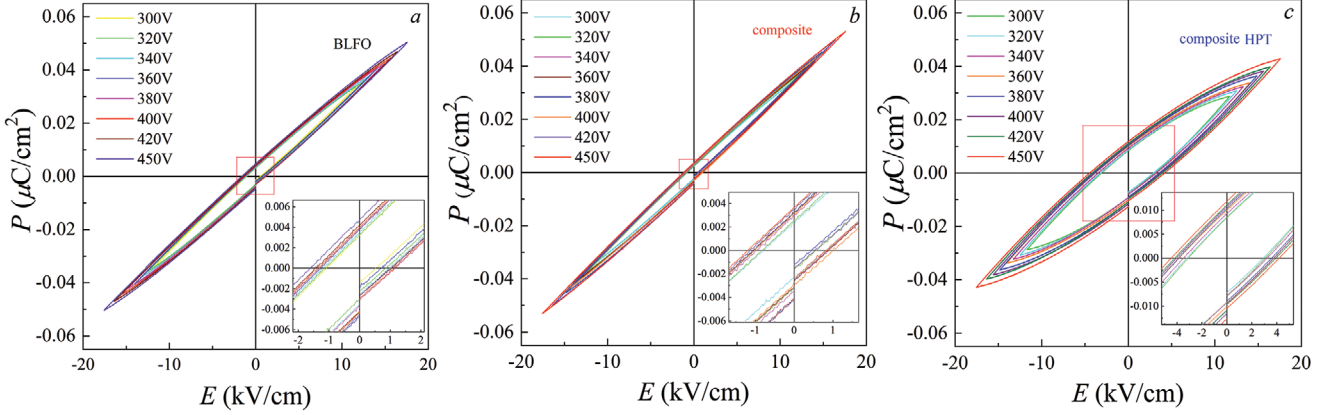
Figure 6. Ferroelectric hysteresis loops for the a) initial BLFO powder, as well as b) the composite and c) composite HPT.

phase. The metamagnetic phase transition is a reorientation process with the "order–order" type phase transition induced by a field, which changes the type of magnetic ordering[35] or an angle between magnetic sublattices in the magnet.[36] The metamagnetic phase transition can be induced not only by external H but also internal H_{int}.[36] As was shown,[37] an additional FM contribution to the magnetization of nanoscale AFM perovskite $BiFeO_3$ with a weak Dzyaloshinsky–Moriya interaction can occur as a result of a spin-reorientation transition induced by the magnetic field. Moreover, this FM contribution depends on both the magnitude of the H and the stress–strain. The FM MZFO fractions in a weak field ≈50 Oe induce large internal fields H_{int} ≈ 5800 Oe. Since the exchange length l_{ex} ≈ 6 nm in the MZFO (Supporting Information 6) exceeds the width of the interfacial boundaries of ≈1 nm and is comparable to the size of ≈14 nm of the BLFO fractions, we can conclude about the existence of exchange interactions between BLFO and MZFO fractions. The presence of exchange interactions, the large H_{int}, and the high stress–strain composite HPT (see Table 1) are the necessary conditions for the spin-reorientation transition in the FM/(AFM+FE) phase,[38] which is the result of an additional FM contribution to the $M_{ZFC}(T)$ dependence. Internal stresses and magnetostriction stabilize FM interactions[39] up to the $T_C^* = 778$ K, above which the BLFO fraction goes into the PM state. An increase in the temperature range of anomalous hysteresis to 795 K is due to spin fluctuations in the frustrated magnetic subsystem of the bismuth ferrite.[40] When the composite is cooled, an additional FM contribution to the $M_{FC}(T)$ is not observed due to the lack of the H_{int}, since the MZFO fractions are in the PM state. The presence of exchange interactions and the irreversible nature of the additional FM contribution to the M is the reason for the appearance of anomalous temperature hysteresis in the temperature range from 671 to 795 K.

The appearance of the exchange-related state between the "strong" FM subsystem and FE phase in the novel composite should lead to a significant increase in the magnetic and electric properties in the range of weak magnetic fields. For this purpose, it is necessary to analyze the hysteresis $P(E)$ curves electronic polarization P in the electric field E and establish that the HPT does not impair the FE properties of the initial BLFO powder.

2.3. P-E Properties

The ferroelectric hysteresis $P(E)$ loops of the initial BLFO powder, as well as the BLFO–MZFO composite processed by compression and HPT at the different E are shown in **Figure 6**. All samples demonstrate the FE behavior for the different applied voltages with a stepwise increase in E up to a maximum value of $E_{max} = 18$ kV cm^{-1}. The choice of E_{max} was not accidentally because of the need to perform the equality of $w_E = w_H$. According to this equality, the energy density of the electric field $w_E = \frac{1}{2}\varepsilon\varepsilon_0 E_{max}^2$ ($\varepsilon_0 = 8.85 \times 10^{-12}$ F m^{-1} is a vacuum permittivity)[41] has to coincide with the energy density of the magnetic field $w_H = \frac{1}{2}BH$ in the field $H = 50$ Oe from the magnetic measurements. A dielectric constant ε equals 80 for the BLFO multiferroic in the electromagnetic field with a frequency of 50 Hz.[42] In the MZFO ferromagnet at the $H = 50$ Oe (3980 A m^{-1}), the induction B is 0.6 T (see 3.2. Magnetic properties). With such values of the ε, B, and H, the equality of $w_E = w_H$ will be performed in the $E \approx 18$ kV cm^{-1} which allows us to compare correctly the mutual influence of ferromagnetic and ferroelectric properties. Additional measurements of frequency dependences of polarization P confirm the absence of a leakage current at a frequency of 50 Hz,[43] which indicates the correct formulation of the experiment, and the definition of $E_{max} = 18$ kV cm^{-1}.

The shape of P-E loops indicates that the E_{max} has not reached the saturation field. The maximum polarization of P_{max} at E_{max}, the residual polarization P_r, and the coercive field E_C with a stepwise increase in the maximum measuring field from 11.7 to 18.0 kV cm^{-1} were defined (**Figure 7**a). In all samples, the linear course of the $P_r(E)$ was found for the entire range of E. In the BLFO powder, the P_{max}, P_r, and E_C are 0.052 µC cm^{-2}, 0.005 µC cm^{-2}, and 1.6 kV cm^{-1}, respectively. In the BLFO–MZFO composite, a slight decrease in the P_r to 0.004 µC cm^{-2} and the E_C to 1.3 kV cm^{-1} is due to a decrease in the FE content of the BLFO phase to 80 wt.%. This conclusion is confirmed by parallel displacement along the ordinate axis of the $P_r(E)$ dependence for the composite (Figure 7a). The increase in the P_{max} from 0.052 to 0.055 µC cm^{-2} is caused by a decrease in the
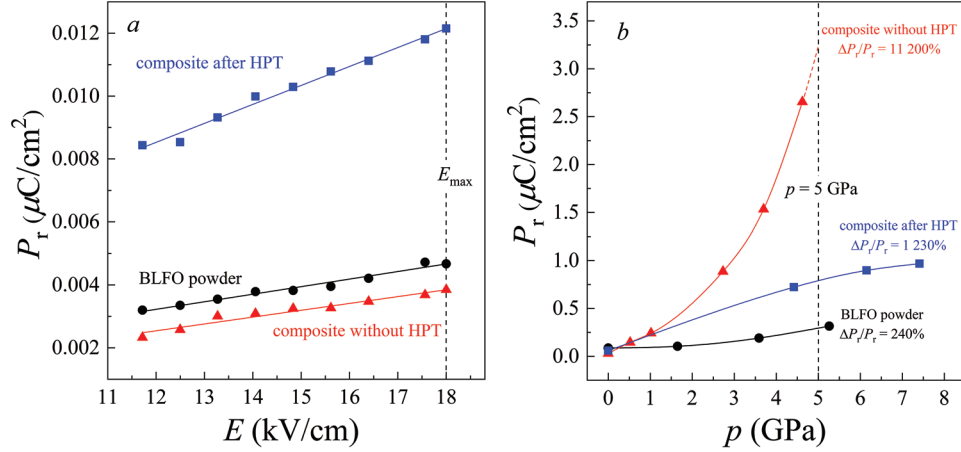
Figure 7. a) The electric field and b) pressure dependences of the residual polarization for the BLFO powder and BLFO–MZFO composite processed by compression and HPT. The $\Delta P_r/P_r$ is a relative change in the pressure-induced residual polarization under 5 GPa.

average particle size of the BLFO in the composite from 131–104 to 103–97 nm (see Table 1). It leads to an increase in the total surface of the FE phase and the accumulation of a weak-connected charge on the boundaries in the low-frequency range.[44] The comparative analysis of P-E loops between the initial BLFO powder and BLFO–MZFO composite (Figure 7a,b) allows us to conclude that the FE properties of the composite are due to the 80 wt.% BLFO fraction and they weakly differ from the properties of the BLFO.

In the BLFO–MZFO composite HPT, there are significant improvements in the FE properties compared to the BLFO powder. Even without considering the decrease in the amount of FE phase in this composite, an increase of 2.4 times in the residual polarization to $P_r = 0.012$ μC cm^{-2} and an increase of 2.9 times in the coercive field to $E_C = 4.6$ kV cm^{-1} are observed. Such a broadening of the hysteresis region is due to an increase in the coupling between magnetic and electric subsystems. The magnetic field induced by the alternating electric field gives an additional contribution to the polarization of the multiferroic in the presence of interaction between FE and FM phases.[45] Reducing the P_{max} by ≈17% to 0.043 μC cm^{-2} is due to the presence of 20 wt.% non-ferroelectric magnetic MZFO fraction in the composite.

Evaluation of the energy density of the electric field w_E for the new composite at room temperature allows us to conclude that a small alternating magnetic field $H \approx 50$ Oe can induce relatively large electric fields ≈18 kV cm^{-1} with an energy ≈3 × 10^{-21} J in the FE fractions with a size of ≈14 nm and with the dielectric constant $\varepsilon \approx 80$. With such properties, the new nanocomposite can become a promising functional material during the creation of high-performance artificial intelligence systems.[46] Such a nanocomposite can dramatically solve the problem of cooling and removing heat in the integrated circuits of high-speed computing systems associated with a decrease in switching energy for nanoscale devices.[47]

The dependences of the effect of high-pressure p on the residual polarization P_r are shown in Figure 7b. From the analysis of the $P_r(p)$ dependences, it can be concluded that there is a significant difference in the effect of p on the FE properties

of the initial BLFO powder and composites. In the BLFO, as p increases from 0 to 5.26 GPa the residual polarization P_r increases by approximately four times to 0.315 μC cm^{-2} with a polarization sensitivity coefficient to 0.043 (μC cm^{-2}) GPa^{-1}. In the BLFO-MZFO composite, there is a colossal increase in the $P_r \approx 92$ times up to 2.654 μC cm^{-2} with an increase in p from 0 up to 4.62 GPa with 0.568 (μC cm^{-2}) GPa^{-1}. In the BLFO-MZFO composite HPT, the residual polarization increases by ≈16 times to $P_r = 0.968$ μC cm^{-2} under $p = 7.41$ GPa with 0.123 (μC cm^{-2}) GPa^{-1}.

For a quantitative assessment of the effect of high-pressure on FE, we have first introduced the relative change of the pressure-induced polarization coefficient $\Delta P_r/P_r = [P_r(p)−P_r(0)]/P_r(0) \times 100\%$ at the same pressure $p = 5$ GPa. This coefficient is $\Delta P_r/P_r = 240\%$ for the BLFO powder, $\Delta P_r/P_r = 11200\%$ for the composite, and $\Delta P_r/P_r = 1230\%$ for the composite HPT (Figure 7b). The large changes in the $\Delta P_r/P_r = 1230\%$ for the BLFO–MZFO composite HPT compared to $\Delta P_r/P_r = 240\%$ for the BLFO powder can be explained by the manifestation of anisotropic nature of piezoelectric properties[48] in the close-packed structure of the composite. However, the colossal change $\Delta P_r/P_r = 11\,200\%$ in the BLFO–MZFO composite requires additional analysis.

An electrical polarization in the BiFeO$_3$ with a rhombohedral R3c distortion of an elementary cell occurs as a result of an anti-phase rotation of the FeO$_6$ octahedra with a displacement of cations of iron and bismuth in one direction and anions of oxygen in another direction.[49] The result of such a local breaking symmetry of the crystal is the appearance of the vector of electrical polarization P along the axis [111]. Applying external high-pressure enhances the deformation of octahedra, changes the angles and the lengths of metal–oxygen bonds, affects the structural properties, and leads to the emergence of new phase transformations.[50]

In the range of external high-pressure from 1.25 to 4.5 GPa for the BiFeO$_3$, several phase transformations associated with the appearance and coexistence of polar R3c rhombohedral (FE), nonpolar P$_{nma}$ orthorhombic (PE, GdFeO$_3$-type), antipolar P$_{bam}$ orthorhombic antiferroelectric (AFE) (PbZrO$_3$-type), and nonpolar I$_{bmm}$ orthorhombic (PE, nonstandard setting of

I_{mma}) phases occurs.[51] In addition to the polarization vector P along the direction [111] in the FE $R3c$ phase, the vector P along the direction in the AFE P_{bam} phase is added.[52] During the coexistence of two different FE phases, a tremendous gain of piezoelectric properties occurs as a result of not only polarization rotation, but also polarization extension near the morphotropic "polar–antipolar" boundary.[53] Pressure-induced phase transformations in the $Bi_{0.9}La_{0.1}FeO_3$ will occur at a lower ≈0.5 GPa external pressure because the chemical pressure during replacing bismuth by 1 mol.% of lanthanum in the $Bi_{1-x}La_xFeO_3$ is approximately equivalent to applying 0.05 GPa hydrostatic pressure on $BiFeO_3$.[54] In the BLFO–MZFO composite, the colossal increase in polarization $\Delta P_r/P_r$ starts at ≈1 GPa (Figure 7b) and coincides with an appearance of the pressure-induced AFE P_{bam} phase.[54] Such a colossal growth of $\Delta P_r/P_r$ is due to an additional contribution to polarization, both from the new AFE P_{bam} phase and from expanding the polarization area near the border between the FE $R3c$ rhombohedral and AFE P_{bam} orthorhombic phases. Additional contribution to pressure-induced growth of $\Delta P_r/P_r$ can give pinning on interfacial "FE/AFE" ($R3c/P_{\text{bam}}$), "FE/PE" ($R3c/P_{\text{nma}}$, $R3c/I_{\text{bmm}}$), and "AFE/PE" ($P_{\text{bam}}/P_{\text{nma}}$, $P_{\text{bam}}/I_{\text{bmm}}$) boundaries.[7a]

Large values of pressure-induced relative changes in the polarization $\Delta P_r/P_r$ for the new composite are of interest and are of great practical importance because such a functional material can be used to create high-pressure sensors. The colossal values of $\Delta P_r/P_r = 11\,200\%$ at 5 GPa make it possible to use the BLFO–MZFO composite as a sensing element in ultrasensitive high-pressure sensors. For creating electronic devices to monitor high-pressure, where the presence of ME coupling in the sensitive element is required, it is advisable to use the BLFO–MZFO composite HPT with $\Delta P_r/P_r = 1230\%$ at 5 GPa and with an almost linear dependence of $\Delta P_r/P_r$ on the pressure in a wide range from 0 to 7.5 GPa.

3. Conclusion

Both new composite materials based on the lanthanum-modified BLFO and MZFO have been obtained without and after the HPT method. The comparative characteristics of their functional properties between each other and with initial BLFO and MZFO powders have been carried out. It has been shown that the nanocomposite HPT is the most close-packed heterophase system consisting of statistically uniformly distributed ultrafine FE BLFO fractions of perovskite with a size of 14 nm and FM MZFO fractions of spinel with a size of 12 nm.
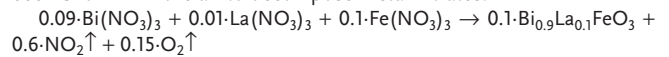
It has been found that the BLFO–MZFO nanocomposite HPT has the unique physical properties of new material: i) an appearance of Curie temperature $T_C = 367$ K near the room temperature; ii) the monotonic change in the coercivity H_C versus T and its small value $H_C \approx 35$ Oe at $T = 300$ K; iii) a decrease in the residual magnetization to $M_r \approx 0.04$–0.4 emu g^{-1}; (iv) an increase of 2.4 times in the residual polarization to $P_r = 0.012$ µC cm^{-2} and an increase of 2.9 times in the field to $E_C = 4.6$ kV cm^{-1}. It has been shown that a small alternating magnetic field of ≈50 Oe has to induce relatively high electric fields of ≈18 kV cm^{-1} with an energy of ≈3×10^{-21} J in the FE fractions of the nanocomposite HPT.

Additionally, for the first time, the FE high-pressure studies of the composites processed by compression and HPT, as well as BLFO powder have been conducted. As turned out, the composite has demonstrated the highest increase in the residual polarization under $p = 5$ GPa.

Thus, we have obtained a multiferroic-like composite with improved magnetic and electric properties, and the used HPT method is an effective and promising method for obtaining new functional materials consisting of close-packed, ultra-dispersed, and exchange-interacting FE and FM phases. Moreover, the degree distribution of fractions, their size, and the strength of exchange interactions can be controlled by both high pressure and the number of revolutions. The obtained new composite can be used for the creation of electronic devices for monitoring ultrahigh pressure and in integrated circuits of high-speed computing systems as a result of a decrease in the switching energy of nanodevices.

4. Experimental Section

The Synthesis of the Bismuth Ferrite $Bi_{0.9}La_{0.1}FeO_3$: The $Bi_{0.9}La_{0.1}FeO_3$ powder was synthesized using the nitrate pyrolysis method. The starting raw materials of $Bi(NO_3)_3\cdot5H_2O$ (99.99% metals basis, Sigma–Aldrich), $La(NO_3)_3\cdot6H_2O$ (99.9% metals basis, Sigma–Aldrich), and $Fe(NO_3)_3\cdot9H_2O$ (99.99% metals basis, Sigma–Aldrich) were dissolved separately in deionized water (75 mL) until a homogeneous solution. The stoichiometric mixture of the obtained solutions was evaporated to dryness in a water bath. The resulting dried powder was preheated at 600 °C for 2 h in the air to decompose metal nitrates:

$0.09\cdot Bi(NO_3)_3 + 0.01\cdot La(NO_3)_3 + 0.1\cdot Fe(NO_3)_3 \rightarrow 0.1\cdot Bi_{0.9}La_{0.1}FeO_3 + 0.6\cdot NO_2\uparrow + 0.15\cdot O_2\uparrow$

The obtaining light brown powder was ground in an agate mortar, placed in an alundum crucible, and calcined in a muffle furnace at 700 °C with isothermal holding for 5 h.

The Synthesis of the Manganese-Zinc Ferrite $Mn_{0.6}Zn_{0.3}Fe_{2.1}O_4$: The $Mn_{0.6}Zn_{0.3}Fe_{2.1}O_4$ powder was prepared by the sol–gel auto-combustion method. The stoichiometric amounts of $Mn(NO_3)_2\cdot4H_2O$ (98%, Sigma–Aldrich), $Zn(NO_3)_2\cdot6H_2O$ (AR, 99%, Sigma–Aldrich), $Fe(NO_3)_3\cdot9H_2O$ (99.99% metals basis, Sigma–Aldrich) were dissolved in deionized water. The appropriate amount of fuel (citric acid monohydrate $H_3Cit\cdot H_2O$, ACS reagent, ≥99.0%) was added to the metal nitrate solution with continuous stirring. The molar ratio of the fuel to the total amount of metal ions (F/M) was set at 1. The final pH was adopted as 7 for better complexing of the metal ions. The pH was adjusted by adding 25 vol.% ammonia solution. The brown sols were heated until the xerogels have been formed. The gel was additionally dried at 120 °C and then rapidly heated at 200 °C to initiate the spontaneous combustion. Finally, the loose ferrite powders were obtained (**Figure 8**).

The Synthesis of BLFO–MZFO Nanocomposite: The BLFO–MZFO nanocomposite was prepared by the HPT method from the powder mixture consisting of 80 wt.% BLFO and 20 wt.% MZFO. The obtained samples were a disk with a diameter of 10 mm and a thickness of 1 mm. These samples were named as BLFO–MZFO composite HPT. The process was carried out in a custom-built HPT installation (W. Klement GmbH, Lang, Austria) with standard semi-constrained anvils (**Figure 9**). The axial pressure 5 GPa was applied, and it was automatically maintained at this level during the experiment. The diameter of the anvil grooves was 10 mm and their total depth was 0.6 mm. The number of the anvils revolutions was 5, while the speed of the rotation was 1 rpm. The experiment was carried out at ambient temperature.

Additionally, the BLFO–MZFO composite was obtained under a pressure of 200 MPa and without torsion. The obtained samples were in the shape of a disk with a diameter of 10 mm and a thickness of 1.5 mm.
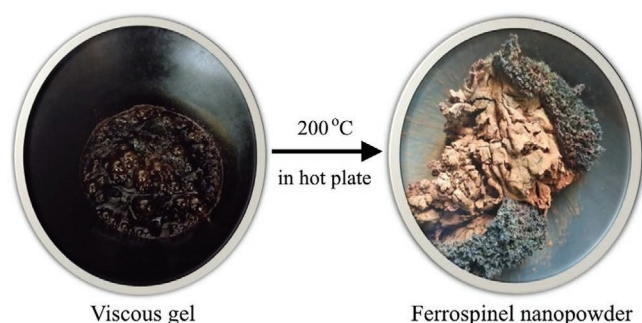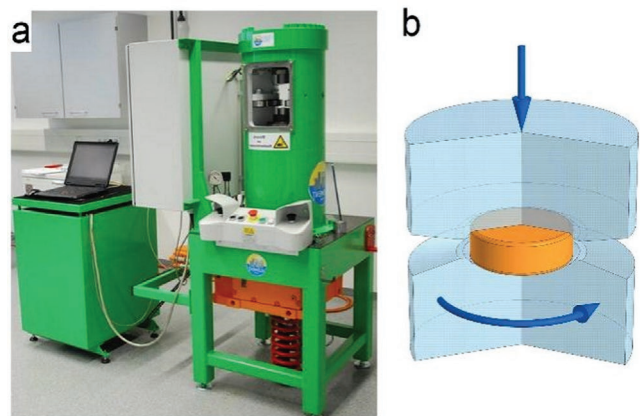
Figure 8. Schematic illustration of ferrospinel nanopowder obtained by sol–gel auto-combustion method.

Methods: The structure symmetry, phase composition, lattice parameters, and the size of the coherent scattering region were determined by the XRD method at room temperature using a Shimadzu Lab XRD 6000 diffractometer in CuK$_\alpha$-radiation (λ_{Cu} = 1.5406 Å). The X-Ray tube was operated at a current of 30 mA and a voltage of 40 kV. The exposure time was 1 s and the measured angle region (2θ) was from 5 to 70°. The scanning step was 0.02°. The structural refinement was performed with Rietveld analysis[55] using the FullProf software.[56]

The morphology and particle size distribution of the BLFO and MZFO powders were determined using FEI MAGELLAN 400 SEM and JEM-2200FS TEM. HRTEM with an accelerating voltage of 200 kV was employed to obtain information about the size and shape of the particles, as well as to determine an average interplanar distance using the FFT approach. The powders for the TEM analysis were prepared by placing a drop of a diluted mixture of particles and acetone on a carbon-coated copper grid. An average particle size D was obtained from analysis of SEM and TEM images within clear and defined particle borders using Nano Measure 1.2.5 software[57] during approximation of the experimental values of D by different distribution functions. It should be noted that obtaining clear images was quite complex due to magnetic attraction between the nanoparticles and their agglomeration in the high-temperature FM ordered MZFO nanopowder (see below Section 3.2). The chemical composition of all samples was performed by EDS using an additional module of FEI MAGELLAN 400.

Magnetic measurements were performed using Quantum Design SQUID MPMS 3 in a wide temperature range from 2 to 900 K and in a magnetic field up to 30 kOe. Measurements of the temperature dependence of magnetization $M(T)$ in a field H = 50 Oe were carried out in two regimes of ZFC and FC. The heating and cooling of samples were conducted with a constant rate equal to 1 K min^{-1}. The temperature relaxation time at the point of measurement was 2 min. The measurement of the field dependence of magnetization $M(H)$ at different temperatures was carried out with an increase in the magnetic field H from 0 to 30 kOe with a step of ΔH = 100 Oe. Additionally, the magnetic measurements under high pressure of p = 1 GPa were performed using a piston-type pressure cell made of Ni–Cr–Al alloy. Silicon oil of low viscosity was used as a pressure-transmitting medium. The pressure inside was measured using the pressure dependence of the superconducting transition temperature of high-purity lead.[58]

The FE properties based on the $P(E)$ hysteresis loops measured in the alternating electric field E at room temperature were studied on a Precision Multiferroic II analyzer equipped with a charge-based magnetoelectric response tester using diamond anvil cell.[57] The gasket with 300 μm in thickness of the pre-indented stainless steel was placed on the symmetric diamond anvil cell with a culet diameter of 400 μm. The ground bulk samples were loaded into a cylindrical hole with a diameter of about 150 μm, together with a few ruby chips for pressure calibration. Two Pt strips were used as electrodes and placed on the surface of the sample. These measurements allow us to obtain $P(E)$ curves for applied maximum voltage of 500 V and frequency of 50 Hz, within the electric field range from −60 kV cm^{-1} to +60 kV cm^{-1}.

Supporting Information

Supporting Information is available from the Wiley Online Library or from the author.

Conflict of Interest

The authors declare no conflict of interest.

Data Availability Statement

The data that support the findings of this study are available from the corresponding author upon reasonable request.

Keywords

high-pressure torsion, magnetic properties, manganese-zinc ferrospinel, multiferroic, polarization properties

Figure 9. The photograph of a) HPT rig and b) the HPT anvil circuit for processing the BLFO–MZFO nanocomposite.

[1] a) W. Eerenstein, N. Mathur, J. F. Scott, *Nature* **2006**, *442*, 759; b) A. C. Garcia-Castro, Y. Ma, Z. Romestan, E. Bousquet, A. H. Romero, *Adv. Funct. Mater.* **2021**, *32*, 2107135.
[2] J. Ma, J. Hu, Z. Li, C. W. Nan, *Adv. Mater.* **2011**, *23*, 1062.
[3] N. Ortega, A. Kumar, J. Scott, R. S. Katiyar, *J. Phys.: Condens. Matter* **2015**, *27*, 504002.
[4] M. M. Vopson, *Crit. Rev. Solid State Mater. Sci.* **2015**, *40*, 223.
[5] T. Rupp, B. D. Truong, S. Williams, S. Roundy, *Materials* **2019**, *12*, 512.
[6] W. Huang, Y. Liu, Z. Luo, C. Hou, W. Zhao, Y. Yin, X. Li, *J. Phys. D: Appl. Phys.* **2018**, *51*, 234005.

[7] a) J. Zhai, Z. Xing, S. Dong, J. Li, D. Viehland, A. P. Letters, **2006**, *88*, 062510; b) G. Mioni, S. Grondin, L. Bardi, F. Stablum, *Behav. Brain Res.* **2020**, *377*, 112232.

[8] V. Pashchenko, A. Khor'yakov, A. Pashchenko, Y. S. Prilipko, A. Shemyakov, *Inorg. Mater.* **2014**, *50*, 191.

[9] M. Bersweiler, P. Bender, L. G. Vivas, M. Albino, M. Petrecca, S. Mühlbauer, S. Erokhin, D. Berkov, C. Sangregorio, A. Michels, *Phys. Rev. B* **2019**, *100*, 144434.

[10] Y. O. Tykhonenko-Polishchuk, A. Tovstolytkin, *J. Nano- Electron. Phys.* **2017**, *9*, 02028.

[11] M. Zhu, Z. Zhou, B. Peng, S. Zhao, Y. Zhang, G. Niu, W. Ren, Z. G. Ye, Y. Liu, M. Liu, *Adv. Funct. Mater.* **2017**, *27*, 1605598.

[12] P. Palmero, *Nanomaterials* **2015**, *5*, 656.

[13] S. B. Waje, M. Hashim, W. D. W. Yusoff, Z. Abbas, *Appl. Surf. Sci.* **2010**, *256*, 3122.

[14] a) V. P. ashchenko, *Powder Metall. Met. Ceram.* **1986**, *25*, 14; b) V. Pashchenko, A. Nesterov, Y. G. Drigibka, G. Potapov, E. Khapalyuk, A. Shemyakov, V. Berezhnaya, *Powder Metall. Met. Ceram.* **1994**, *33*, 300; c) V. Pashchenko, A. Nesterov, Y. G. Drigibka, G. Potapov, E. Khapalyuk, A. Shemyakov, V. Berezhnaya, *Powder Metall. Met. Ceram.* **1995**, *33*, 300.

[15] a) R. Kulagin, Y. Beygelzimer, Y. Ivanisenko, A. Mazilkin, H. Hahn, *Proc. Eng.* **2017**, *207*, 1445; b) P. W. Bridgman, *Phys. Rev.* **1935**, *48*,825; c) A. P. Zhilyaev, T. G. Langdon, *Prog. Mater. Sci.* **2008**, *53*, 893.

[16] a) A. Pashchenko, V. Pashchenko, Y. F. Revenko, V. Spuskanyuk, N. Kasatka, V. Turchenko, A. Shemyakov, *Tech. Phys. Lett.* **2010**, *36*, 566; b) Y. Beygelzimer, Y.i Estrin, A. Mazilkin, T. Scherer, B. Baretzky, H. Hahn, R. Kulagin, *J. Alloys Compd.* **2021**, *878*, 160419; c) Y. Ivanisenko, R. Kulagin, V. Fedorov, A. Mazilkin, T. Scherer, B. Baretzky, H. Hahn, *Mater. Sci. Eng., A* **2016**, *664*, 247.

[17] a) K. Edalati, Z. Horita, *Scr. Mater.* **2010**, *63*, 174; b) H. Razavi-Khosroshahi, K. Edalati, M. Hirayama, H. Emami, M. Arita, M. Yamauchi, H. Hagiwara, S. Ida, T. Ishihara, E. Akiba, Z. Horita, M. Fuji, *ACS Catal.* **2016**, *6*, 5103; c) B. Ifa, A. Pe, A. Qw, A. Mw, B. Ma, B. Sm, C. Tia, A. Ke, *Scr. Mater.* **2020**, *187*, 366.

[18] R. Blaak, *J. Chem. Phys.* **2000**, *112*, 9041.

[19] a) A. Patterson, *Phys. Rev.* **1939**, *56*, 978; b) B. Warren, *J. Appl. Phys.* **1941**, *12*, 375.

[20] A. S. Abramov, D. O. Alikin, V. V. Yuzhakov, A. N. Nikitin, S. I. Latushko, D. V. Karpinsky, V. Y. Shur, A. L. Kholkin, *Ferroelectrics* **2019**, *541*, 1.

[21] A. Okada, Y. Yamamoto, T. Yoshiie, I. Ishida, K. Hamada, E. Hirota, *Mater. Trans., JIM* **1993**, *34*, 343.

[22] M. Zhang, Z. Zi, Q. Liu, P. Zhang, X. Tang, J. Yang, X. Zhu, Y. Sun, J. Dai, *Adv. Mater. Sci. Eng.* **2013**, *2013*, 609819.

[23] M. T. Varshavskii, V. P. Pashchenko, A. N. Men, N. V. Suntsov, A. G. Miloslavskii, in *Defect Structure and Physicochemical Properties of Ferrospinels [in Russian]*, Nauka, Moscow **1988** p. 244.

[24] S. Mørup, M. F. Hansen, C. Frandsen, *Beilstein J. Nanotechnol.* **2010**, *1*, 182.

[25] P. Suresh, S. Srinath, *J. Alloys Compd.* **2013**, *554*, 271.

[26] D. Albrecht, S. Lisenkov, W. Ren, D. Rahmedov, I. A. Kornev, L. Bellaiche, *Phys. Rev.* **2010**, *81*, 140401.

[27] a) H. FD., https://www.ferroxcube.com/en-global/download/download/11 **2009**; b) H. M. L., MaDC-F, http://www.hitachi-metals.co.jp/e/products/elec/tel/p13_21.html **2020**.

[28] K. P. Belov, *Physics-Uspekhi* **1996**, *39*, 623.

[29] A. Guimaraes, Springer-Verlag Berlin Heidelberg: Wiley-IEEE Press, **2009**.

[30] S. Krupička, *Physik der Ferrite und der verwandten magnetischen Oxide*, Springer-Verlag, Prag **2013**.

[31] M. Opel, *J. Phys. D: Appl. Phys.* **2012**, *45*, 033001.

[32] D. Venkateshvaran, M. Althammer, A. Nielsen, S. Geprags, M. S. Ramachandra Rao, S. T. B. Goennenwein, M. Opel, R. Gross, *Phys. Rev. B* **2009**, *79*, 134405.

[33] A. Perejon, P. E. Sanchez-Jimenez, L. A. Perez-Maqueda, J. M. Criado, J. R. de Paz, R. Saez-Puche, N. Maso, A. R. West, *J. Mater. Chem. C* **2014**, *2*, 8398.

[34] Y. M. Gufan, V. M. Kalita, *Fiz. Tverd. Tela* **1987**, *29*, 3302.

[35] G. Y. Lavanov, V. Kalita, V. Loktev, *Low Temp. Phys.* **2014**, *40*, 823.

[36] G. R. Hoogeboom, T. Kuschel, G. E. Bauer, M. V. Mostovoy, A. V. Kimel, B. J. van Wees, *Phys. Rev. B* **2021**, *103*, 134406.

[37] a) R. Levitin, A. S. Markosyan, *Soviet Physics Uspekhi* **1988**, *31*, 730; b) X. X. Shi, X. Q. Liu, X. M. Chen, *Adv. Funct. Mater.* **2017**, *27*, 1604037.

[38] Z. Gareeva, A. Zvezdin, L. Kalyakin, T. Gareev, *J. Magn. Magn. Mater.* **2020**, *515*, 167255.

[39] H. Dixit, J. H. Lee, J. T. Krogel, S. Okamoto, V. R. Cooper, *Sci. Rep.* **2015**, *5*, 12969.

[40] J.-G. Park, M. D. Le, J. Jeong, S. Lee, *J. Phys.: Condens. Matter* **2014**, *26*, 433202.

[41] H. A. Haus, J. R. Melcher, *Electromagnetic fields and energy*, Prentice Hall Englewood Cliffs, NJ, **1989**.

[42] A. Pashchenko, N. Liedienov, Q. Li, I. Makoed, D. Tatarchuk, Y. Didenko, A. Gudimenko, V. Kladko, L. Jiang, L. Li, *Mater. Chem. Phys.* **2021**, *258*, 123925.

[43] H. Naganuma, Y. Inoue, S. Okamura, *J. Ceram. Soc. Jpn.* **2010**, *118*, 656.

[44] a) A. Pashchenko, N. Liedienov, Q. Li, D. Tatarchuk, V. Turchenko, I. Makoed, V. Y. Sycheva, A. Voznyak, V. Kladko, A. Gudimenko, *J. Magn. Magn. Mater.* **2019**, *483*, 100; b) N. Liedienov, A. Pashchenko, V. Turchenko, V. Y. Sycheva, A. Voznyak, V. Kladko, A. Gudimenko, D. Tatarchuk, Y. V. Didenko, I. Fesych, *Ceram. Int.* **2019**, *45*, 14873; c) I. I. Makoed, N. A. Liedienov, A. V. Pashchenko, G. G. Levchenko, K. I. Yanushkevich, *J. Alloys Compd.* **2020**, 155859.

[45] E. Elayaperumal, G. Murugesan, M. Malathi, *Mater. Lett.* **2021**, *300*, 130048.

[46] R. Ramesh, L. Martin, *Riv. Nuovo Cimento* **2021**, *44*, 251.

[47] V. V. Zhirnov, R. K. Cavin, *Nat. Nanotechnol.* **2008**, *3*, 77.

[48] a) J. Lv, X. Lou, J. Wu, *J. Mater. Chem. C* **2016**, *4*, 6140; b) X. Ming, X. Meng, Q.-L. Xu, F. Du, Y.-J. Wei, G. Chen, *RSC Adv.* **2014**, *4*, 64601.

[49] F. Kubel, H. Schmid, *Acta Crystallogr., Sect. B: Struct. Sci.* **1990**, *46*, 698.

[50] a) G. Zhang, F. Liu, T. Gu, Y. Zhao, N. Li, W. Yang, S. Feng, *Adv. Electron. Mater.* **2017**, *3*, 1600498; b) C. Xu, Y. Li, B. Xu, J. Íñiguez, W. Duan, L. Bellaiche, *Adv. Funct. Mater.* **2016**, *27*, 1604513; c) J. Chen, B. Xu, X. Q. Liu, T. T. Gao, L. Bellaiche, X. M. Chen, *Adv. Funct. Mater.* **2018**, *29*, 1806399.

[51] a) A. A. Belik, H. Yusa, N. Hirao, Y. Ohishi, E. Takayama-Muromachi, *Chem. Mater.* **2009**, *21*, 3400; b) V. Khomchenko, D. Karpinsky, A. Kholkin, N. Sobolev, G. Kakazei, J. Araujo, I. Troyanchuk, B. Costa, J. Paixao, *J. Appl. Phys.* **2010**, *108*, 074109.

[52] D. C. Arnold, *IEEE trans. ultrason. ferroelectr. freq. control* **2015**, *62*, 62.

[53] D. Damjanovic, *Appl. Phys. Lett.* **2010**, *97*, 062906.

[54] C. S. Knee, M. G. Tucker, P. Manuel, S. Cai, J. Bielecki, L. Börjesson, S. G. Eriksson, *Chem. Mater.* **2014**, *26*, 1180.

[55] H. M. Rietveld, *J. Appl. Crystallogr.* **1969**, *2*, 65.

[56] J. Rodríguez-Carvajal, *Phys. B* **1993**, *192*, 55.

[57] Z. Wei, A. Pashchenko, N. Liedienov, I. Zatovsky, D. Butenko, Q. Li, I. Fesych, V. Turchenko, E. Zubov, P. Y. Polynchuk, *Phys. Chem. Chem. Phys.* **2020**, *22*, 11817.

[58] a) V. P. Dyakonov, G. G. Levchenko, R. Journ, *Instrum. Exp. Tech.* **1983**, *5*, 236; b) M. Baran, V. Dyakonov, L. Gtadczuk, G. Levchenko, S. Piechota, H. Szymczak, *Physica C: Supercond.* **1995**, *241*, 383.